In-situ shrinkage measurement of alkali-activated materials using focused ion beam combined with environmental scanning electron microscopy

Zhonggou Chen [a], Hua Ding [b,*], Guoyi Zhang [a,**], Pingtai Chai [c]

[a] *School of Landscape Architecture, Zhejiang Agriculture and Forestry University, Hangzhou, 311300, China*
[b] *Shaoxing Zhenghao Engineering Testing Co., Ltd, China*
[c] *Zhejiang Shilang Longshan Engineering Design Co., Ltd, China*

ARTICLE INFO

ABSTRACT

Drying shrinkage of alkali-activated slag (AAS) has gained significant attention since the volumetric instability of this material can generate premature cracking and degrade the long-term durability of concrete structures. The unique shrinkage behavior of AAS originates mainly from the particular characteristics of its main hydrated products. However, few studies have even attempted to investigate the shrinkage behavior of hydrated products in AAS materials. This paper presented a new method of investigating drying shrinkage behavior of AAS using focused ion beam (FIB) combined with environmental scanning electron microscopy (ESEM). This innovative experimental method allowed the in-situ measurement of phase-specific shrinkage. The results showed FIB/ESEM technique can be successfully implemented to cementitious material to prepare phase-specific samples. Furthermore, object-oriented finite element method (OOF2) has been utilized to compute the shrinkage behavior of AAS concrete using a proposed multi-scale scheme. The computations can be made at multi-scales which highlight the effect of hydration products on shrinkage behaviors. OOF2 calculation at the micro-length scale predicted an increase in the shrinkage due to the well-dispersed hydration products inside the matrix. At larger scale, the decrease in the overall shrinkage is related to the extremely low shrinkage value by aggregates. The findings reveal OOF2 offers the capability to accurately measure local stress and strain distribution within heterogeneous materials, a feature notably absent in conventional numerical homogenization approaches. The importance of this benefit is highlighted particularly in the context of free-restrained shrinkage prediction, as conventional homogenization methods fail to account for stress.

1. Introduction

Volumetric instability of cementitious materials can cause serious problems in infrastructure by affecting its long-term durability through generating premature cracking [1–3]. Despite the growing interest in cement-free materials due to environmental concerns and the economic need for effective reuse of industry byproducts, these materials often suffer from inadequate volumetric stability. For

instance, alkaline activated slag (AAS), one of the most promising alternatives to ordinary Portland cement (OPC), was widely reported to have considerably higher shrinkage than OPC, and showed significant cracking tendency [4–8]. However, the mechanism of shrinkage for AAS remains unclear, although it was generally acknowledged to be associated with its uniform gel products and pore structure [5,6,9,10]. To enhance our understanding of Alkali-Activated Slag (AAS) shrinkage, prior studies have focused on accurately assessing drying shrinkage through macro-length measurements [6]. However, the majority of previous macro-length measurements on drying shrinkage were apparent shrinkage, which is strongly dependent on the geometry of specimens. The true shrinkage should be a result of merely moisture gradients that occurs during drying process regardless of geometry [11–13]. Additionally, for the purpose of simulating stress development induced by shrinkage gradients in concrete, the correlation between local true shrinkage and RH is also essential [14]. In order to compute the true shrinkage of cementitious material, a very tiny and thin sample is typically a requisite pre-requirement. Some researchers have conducted a series of experimental procedures to measure and calculate the true shrinkage of cement paste using environmental scanning electron microscopy (ESEM) [11,15]. However, neither macro-length nor paste-ESEM-based measurement accounts for the heterogeneous nature of cementitious materials.

As shown in Fig. 1, similar to cement paste, AAS paste (Level I) is also a heterogeneous composite material containing unhydrated slag, various hydrate products (gel, hydrotalcite, AFm phases), and capillary pores. It should be noted that microstructure of AAS depends on activator and curing condition, and silicate-activated slag tends to form more homogenous microstructure which is also the activator adopted in this paper. Each phase within this microstructure has a different shrinkage response. For instance, it is likely that calcium-aluminosilicate-hydrate gel (C-A-S-H) shrinks most, while unhydrated slag and crystalline phase restrain this shrinkage. It is probable that the uniform shrinkage characterization of C-A-S-H gel in AAS contributes inherently to its apparent large macroscopic shrinkage [16]. Therefore, understanding the actual shrinkage behavior of C-A-S-H gel, along with its proportion and distribution, is crucial for accurately predicting macroscopic shrinkage [16]. However, quantifying the true shrinkage-RH response of C-A-S-H is extremely difficult to be obtained since in realistic hydrated products, several different types of hydrate products are deeply mixed and intertwined with each other, making it impossible to be identified separately. Although it is possible to shed some light on the shrinkage behavior by using synthesized C–S–H gels, the results and conclusions may not be straightforwardly applicable to realistic cases due to its considerable simplification. Also, the shrinkage of C-A-S-H gel would depend on its composition and porosity, which in turn are affected by the mixing proportions and chemical composition of slag, and the material processing techniques (e.g., type/-dosage of alkali-activator, curing regime). Admittedly, this information cannot be obtained by macroscopic shrinkage measurement, which actually describes the overall properties on average aspects. Whilst at mesoscopic scale (Level II), AAS mortar or concrete contains AAS paste, aggregate, and interfacial transition zone (ITZ). At this scale, overall paste shrinkage might be restrained by aggregates within the composite, which induce micro-cracking in paste or ITZ.

As a highly heterogeneous composite at multi-scale as introduced above, predicting the drying shrinkage of AAS concrete is extremely complicated. Nowadays, the concept of representative volume element (RVE) is intensively utilized by many researchers to
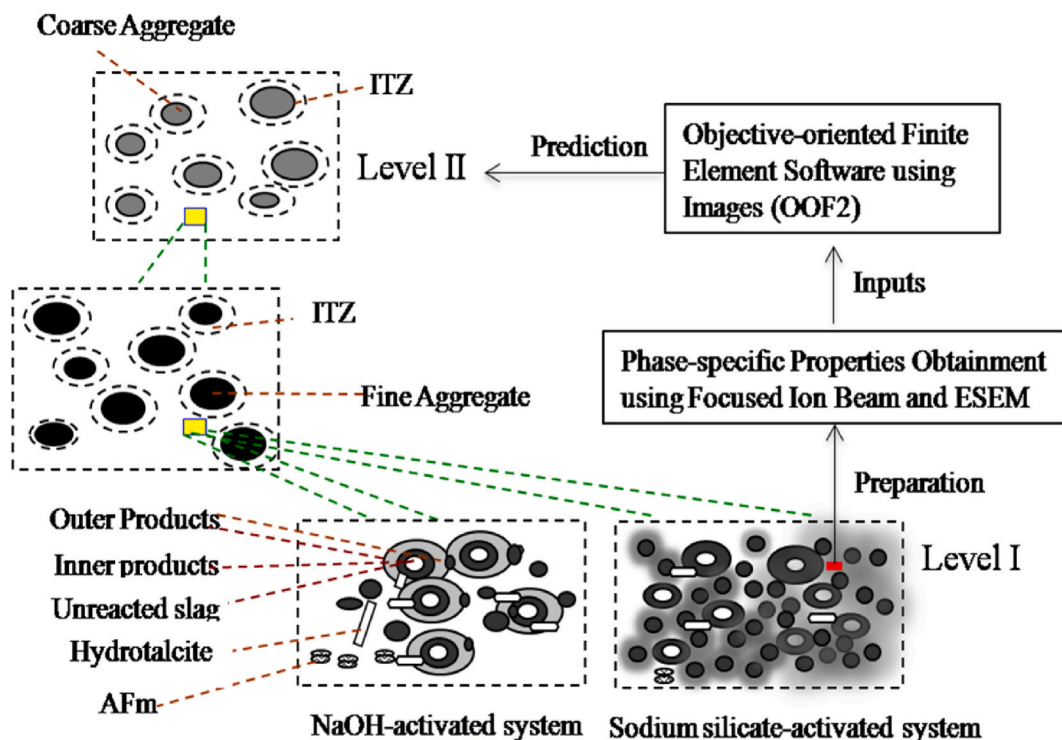

Fig. 1. Realization of multi-scale modeling for alkaline activated slag system.

bridge the large gap between different scales using multi-scale models and micromechanical framework via homogenization, which is realized mainly by multiple micromechanical approaches (e.g. Mori-Tanaka method, self-consistent scheme) that seeks to identify effective properties by solving matrix-inclusion problems. While the mean-field approximation using a statistically representative microstructure offers useful limits for calculating materials' effective properties and responses (such as predicting large, visible cracks but not micro-cracking behavior), it often overlooks crucial geometrical data. This is particularly evident when macroscopic properties non-linearly depend on underlying attributes, or when the properties of interest emerge from the extremes of a distribution. For example, in the case of AAS concrete, aggregate-restrained shrinkage might depend on the presence of aggregates and vary with their distribution and geometrical shapes. In other words, a mean-filed based approximation may be inappropriate to simulate the drying shrinkage if interest is particularly on the detailed microstructure itself instead of the overall behaviors.

To address these research challenges, two main attempts towards multi-scale shrinkage simulation were made in this paper: sub-micro-scale shrinkage observation and measurement, as well as object-oriented multi-scale simulation. More specifically, there are two major objectives in this work. First, this study proposes an innovative method for sampling the hardened AAS paste microstructure to allow phase-specific shrinkage and compositional measurements, primarily using a focused ion beam (FIB) combined with environmental SEM. On the other hand, the object-oriented finite (OOF2) element developed by the National Institute of Standards and Technology (NIST) was utilized in the present study to simulate the shrinkage behavior of AAS at multi-scales. The computational framework of the present study is shown in Figs. 1 and 2 and is elaborated in the methodology section. In addition, since much attention has been paid previously to the aggregate-restrained shrinkage behavior and simulation (on Level II) [17–20], the present study mainly focuses on the Level I problem and the gap-establishing issues between Level I and Level II since the methodology is analogous in each dimension.

2. Materials and methods

2.1. Materials and mixing proportion

A commercial ground granulated blast-furnace slag with a density of 2.89 g/cm^3 was used in this study. The median particle size (D_{50}) of slag is 12 μm, and its main oxide composition is as follows: 43.8 % CaO, 30.0 % SiO$_2$, 12.7 % Al$_2$O$_3$, and 4.8 % MgO. The slag was activated with a combination of sodium hydroxide (NaOH) and sodium silicate solution (the composition of sodium silicate solution is Na$_2$O·(SiO$_2$)$_{1.6}$·(H$_2$O)$_{10}$, density is 1.60 g/cm^3, pH is 13.7) which maintains a SiO$_2$/Na$_2$O molar ratio of 1.22. The mass ratio of NaOH solution and sodium silicate solution was 2.2. The NaOH solutions (with a concentration of 2.86 %) were prepared using pellets with a specific gravity of 2.13 g/cm^3. To create the activating solutions, NaOH pellets were dissolved in water at room temperature in a sealed beaker to prevent carbonation and evaporation. The mixture was shaken for 5 min and then left to stand for about 2 h to dissipate heat and return to room temperature. For the Alkali-Activated Slag (AAS) mortar specimens (Level II), natural sands with a fineness modulus of 2.60, an oven-dry specific gravity of 2.52, and an absorption capacity of 2.0 % were used. In addition, a small dosage (about 1 % of binder) of a high-range water-reducing admixture was added to AAS systems to ensure good workability. The
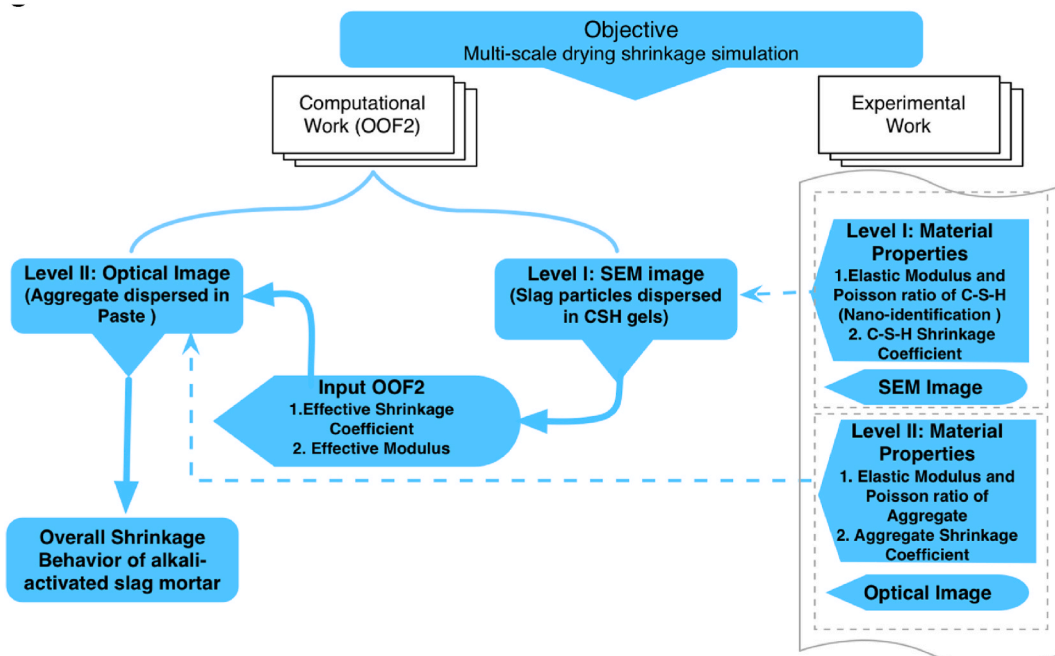

Fig. 2. Flowchart summarizing the methodology used in simulating drying shrinkage behavior of alkali-activated slag mortar and concrete.

dosage of activators was selected to obtain the volumetric liquid-to-slag ratio of 1.30. Furthermore, the AAS mortar mixture was formulated to contain 50.7 % sand by volume. Once all ingredients were ready for mixing, all specimens were mixed and compacted according to ASTM C305 specifications. More specifically, the slag was first placed in the mixing bowl, followed by pouring the activating solution and dry sand. After casting, all specimens were cured at 23 ± 0.5 C, 100 % RH for 7 days until the tests.

2.2. FIB preparation of the sub-microscale solids formed in AAS

After the AAS sample was moisture cured, a similar procedure to SEM sample preparation was performed. The detailed experimental procedure for SEM can be found in the literature. It should be noted that either SEM or FIB preparation operates in a high vacuum but can work under cryogenic conditions. As such, the paste samples need to be cross-sectioned at dry or frozen conditions. In the first case, solvent exchange drying was used to minimize irreversible shrinkage by immersing the crushed sample in methane liquid for about 7 days. After the sample was polished and coated with a layer of carbon, it is ready to be performed by FIB. The primary reason for using Focused Ion Beam (FIB) is its sputtering/milling capability, enabling the preparation of a microscopic cross-section (slab) specimen. Owing to its diminutive size, this slab can be crafted to predominantly consist of a single microstructure phase. In the case of this investigation, the hydrate products, mainly composed of C–S–H gel, is selected to be the objective phase. As illustrated in Fig. 3, a finely focused (10 nm) Ga + ion beam mills two triangular trenches on the surface of an AAS sample. The progress of trenching is carefully controlled using simultaneous SEM. The angle between SEM and FIB is titled 52°. The prepared FIB specimen is shown in Fig. 4(a) and **(b)**.

2.3. Drying shrinkage measurement in ESEM

The FIB-prepared AAS cross-section was further used for measuring the true unrestrained phase-specific shrinkage-RH response of hydrate constitutes. For this purpose, the slab specimen was studied inside an environmental SEM, which is capable of controlling the ambient RH under which the sample is subjected. The desired RH was controlled by varying the pressure at a constant temperature (20 °C). This technique was previously proposed by Neubauer et al. [15] to measure strain using a fracture SEM image of cement paste but has never been applied to FIB cross-sections or AAS materials. The ESEM images were captured at every RH step (e.g. 100 %, 70 %, 60 %, 40 %, 20 % and 10 % RH in this study), and an image analysis was used to monitor the movement of a grid of virtual nodes on the slab specimens and thus, to determine the true shrinkage strains. In parallel, compositional X-ray (EDS) analysis allows correlating shrinkage response to phase compositions. It should be noted that as the samples are very thin, it reached hydroscopic equilibrium quicky. Therefore, the duration of drying equilibrium was controlled to be at least 1 h, before imaging.

3. Shrinkage behavior of sub-micro-scale solids formed in AAS

Fig. 5 shows the secondary electron image of FIB sample under different RHs as measured by Environmental SEM. The magnification for all images was 15000×. It can be seen that higher shrinkage can be observed at lower RH range compared with that at high RH. In order to further quantify the drying shrinkage at different RHs, image correlation (IC) method [21] is performed. The IC method delivers a comprehensive in-plane deformation field of the planar specimen's surface by comparing BSE images taken at varying RHs. As mentioned before, the thickness of FIB sample is less than 600 nm, under which the deformation takes place in 2D planar. Fig. 6 illustrates the fundamental principle of the 2D IC method: it involves matching identical pixels in images captured before and after deformation. To calculate the displacements at a specific point P, a square reference subset centered at P is selected from the initial image and is used to locate its equivalent in the deformed image. Once this target subset's position is identified in the deformed image,
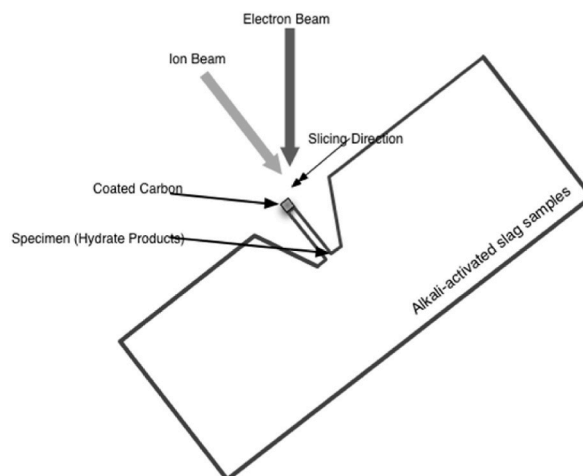

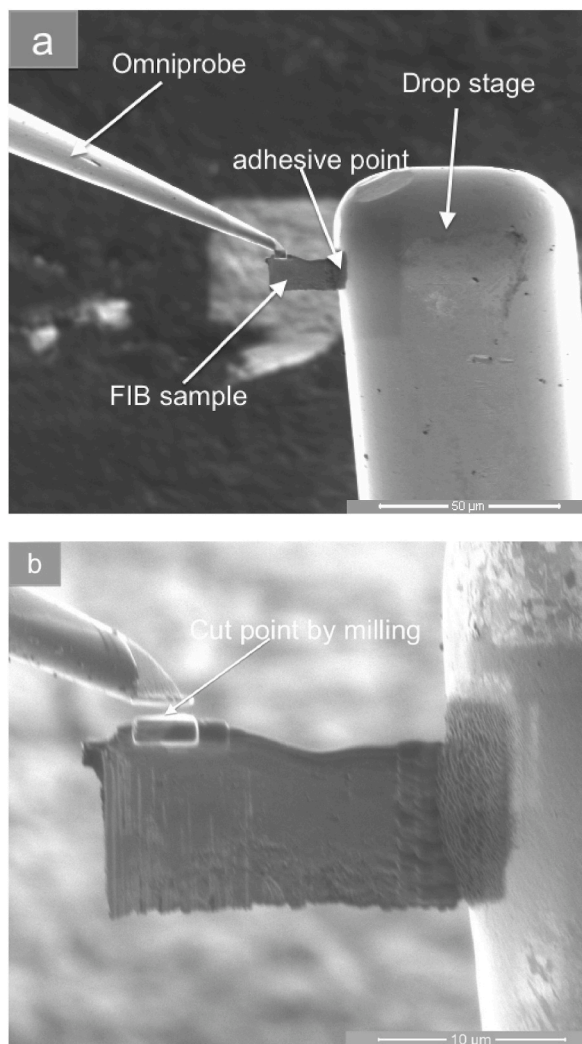**Fig. 3.** Overview of the principal method used to prepare a FIB sample for shrinkage investigation.

Fig. 4. Finishing the FIB procedure by putting the lift-out samples on a drop stage and doing the final clean milling (a) making the sample attached to the drop stage using Omniprobe; (b) Cutting the adhesive point using milling.

the displacement components at the centers of both the reference and target subsets are determined. This process is repeated across virtual grids to map the entire deformation field. From this, the strain field is derived based on the deformation data. For more comprehensive details on the IC method, numerous literature sources are available [21,22]. In the present case, the drying shrinkage strain distributions are calculated using the Matlab code for correlating the reference undeformed image (100%RH) with that of the deformed image [23].

Fig. 7 shows the computed shrinkage strain distribution at different RHs, and Fig. 8 shows the overall shrinkage deformation changes at different RHs. Upon 100 % RH to 40 % RH, the shrinkage increases slowly, then reaches a peak at about 20 % RH, and then slightly decreases at 10 % RH. The reduction in shrinkage at 10 % RH is probably due to the release of capillary pressure exerted on C–S–H gel skeleton when water is evaporated further. The highest shrinkage strain computed here is about 0.1 % at 20 % RH. However, the true shrinkage strain shown in Fig. 8 demonstrates that the maximum true shrinkage strain at various RHs ranges from ±0.1 to ±0.2. It demonstrates that there is a competition between the shrinkage and expanding of the specimens, which controls the overall shrinkage deformation. At high RH range, the overall shrinkage increases as more small deformation regions increases. While at lower RH range, the magnitude of deformation at original regions enlarges. Simultaneously the magnitude of expanding parts also increases as well. It makes quantifying the shrinkage behavior of C–S–H solid complicated. Admittedly, the relative proportion of the shrinkage and expanding parts and their individual magnitude control the overall shrinkage deformation. This complicated phenomenon needs further investigation and a single parameter is impossible to represent its shrinkage characteristics.

Additionally, the measured short-term drying shrinkage of AAS is relatively smaller at high relative humidity (RH) range than with that at the lower RH range. Compared with long-term shrinkage test results for the same batch of material, it is probable that creep is likely to play an important role in the drying deformation of AAS although a thin sample is implemented in this study. Previous
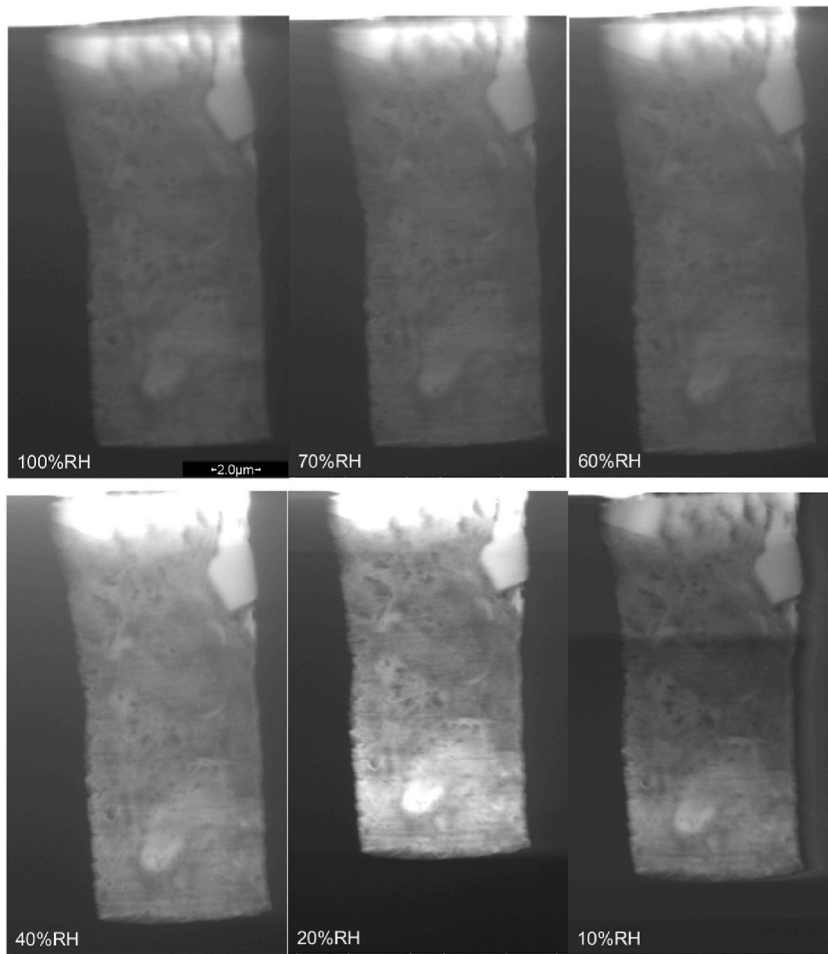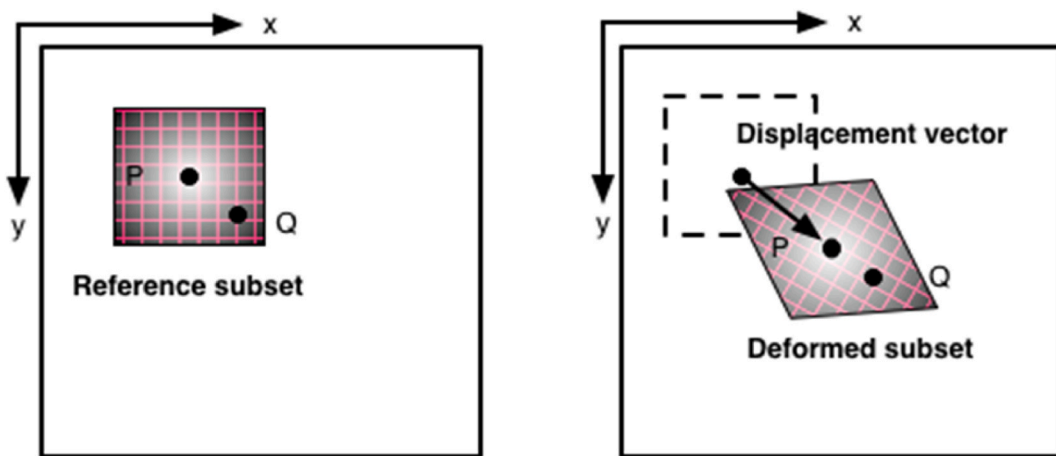
Fig. 5. SE image of FIB sample under different RHs as measured by environmental scanning electron microscopy.

(a) Reference square subset of reference image　　**(b) Deformed subset of deformed image**

Fig. 6. The basic principle of image correlation method (modified from Refs. [21,22]).
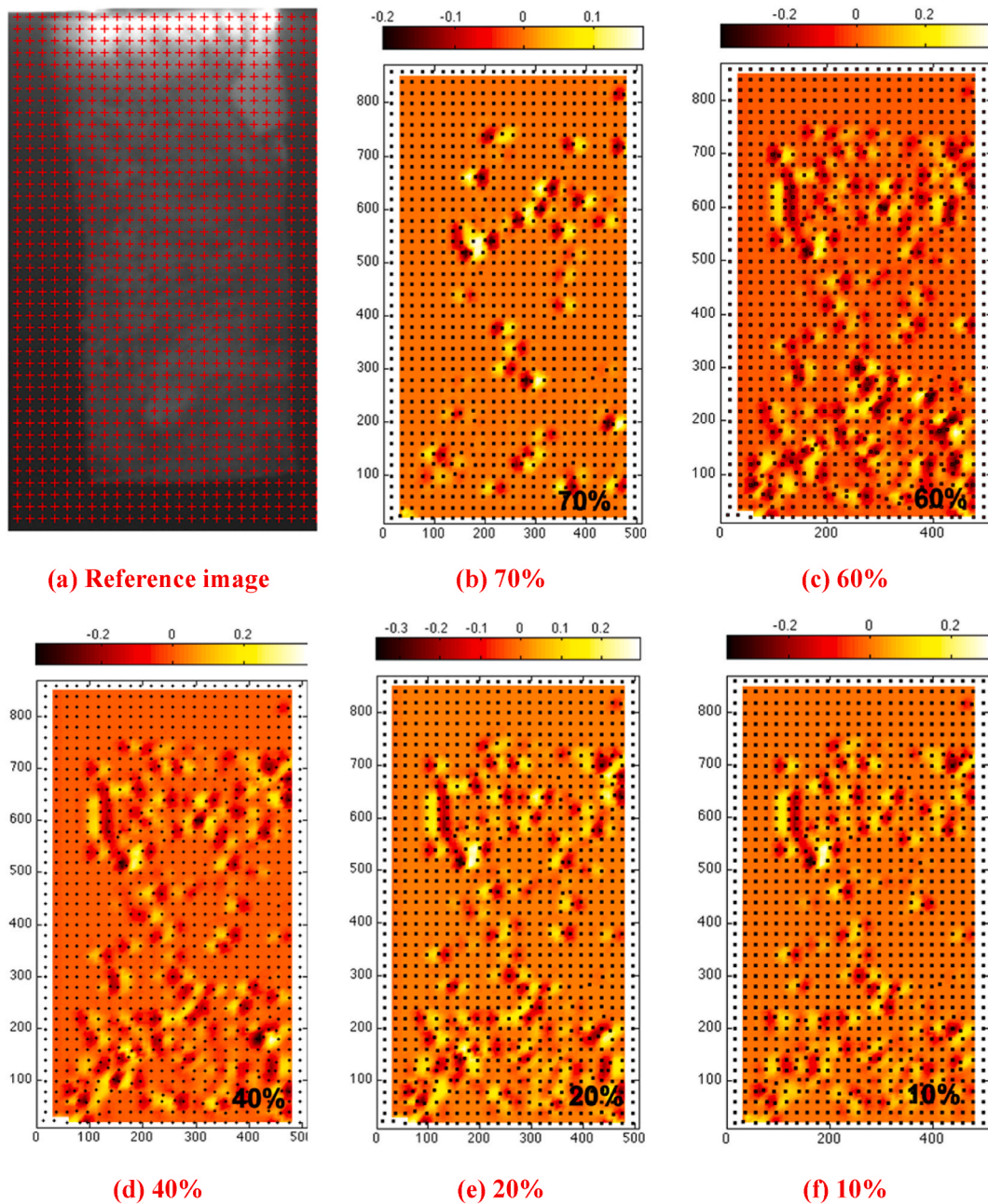
Fig. 7. Reference image, the imposed red point is used for tracking the motion of images and the calculated strain imposed on the deformed image under various RHs.

research regarding the creep mechanism of C–S–H gel shows that creep is likely an aging process [24] which may not be realized solely using thin sample although the equilibrium is quickly reached. The result indicates that short-term shrinkage measurement of AAS is not comparable to that of long-term, but provides additional evidence that high shrinkage of AAS is a result of longer-term deformation.

4. Object-oriented finite element simulation

4.1. OOF2

OOF2 is a unique coding method that transforms digitized images of microstructures, like SEM micrographs, into finite element
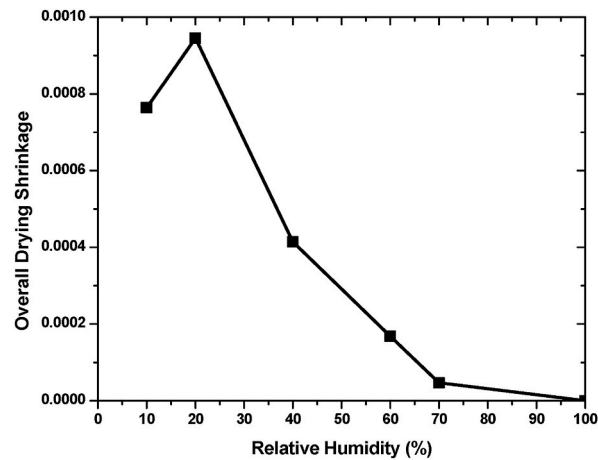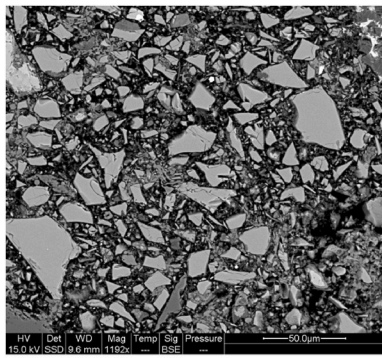
Fig. 8. Image correlation analysis for SE images obtained under different RHs for overall drying shrinkage.

meshes. It can directly apply specific material properties (such as shrinkage coefficient, elastic modulus) to different components of the microstructure image, including unhydrated slag, hydration products, and aggregate, as discussed in this paper. The resulting finite element model comprehensively represents microstructural characteristics, encompassing volume fraction, shape, orientation, size, and spatial distribution of inclusions. This method facilitates the analysis of how microstructure features influence the macroscopic behavior of materials through multi-scale techniques. As a consequence, the measured shrinkage behavior of the sub-micro-scale solids formed in the AAS can be incorporated into a microscopic scale (i.e. AAS paste) to simulate shrinkage behavior. Furthermore, the computed microscopic shrinkage behavior can be further incorporated into the macro-scale shrinkage simulation framework. In
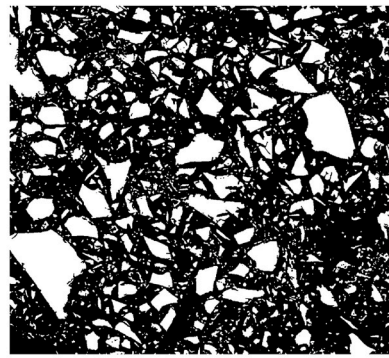
Table 1
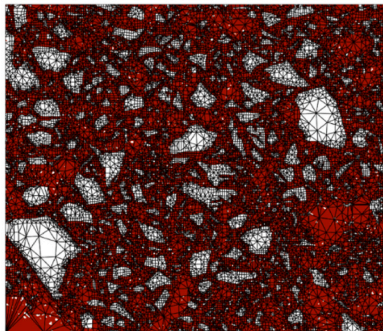Elastic modulus of cementitious material phases obtained using nano-indentation as reported in the literature.

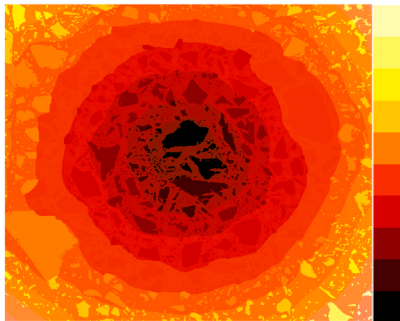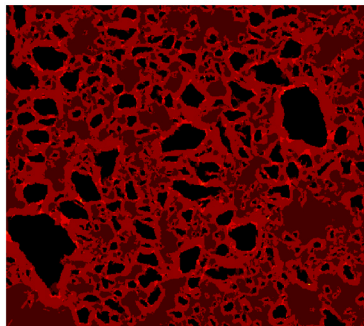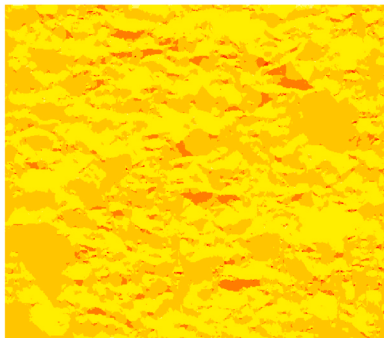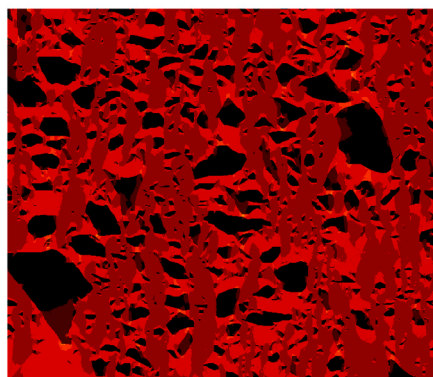| Type	Phase	Er (GPa)	SD	Activator	Reference
Alkali-activated Slag	LD-C-A-S-H	25.02	5.53	5M-NH	[25]
		25.47	5.82	8M-NH	[25]
		28.64	4.11	12M-NH	[25]
	HD-C-A-S-H	41.42	3.56	5M-NH	[25]
		40.20	3.76	8M-NH	[25]
		41.55	3.78	12M-NH	[25]
	Unhydrated Slag	77.60	17.12	5M-NH	[25]
		70.14	15.43	8M-NH	[25]
		70.11	14.30	12M-NH	[25]
	C-A-S-H	27.81	10.73	1.5M-NS	[25]
		30.27	10.06	2.5M-NS	[25]
	Unhydrated Slag	80.03	23.96	1.5M-NS	[25]
		85.14	23.61	2.5M-NS	[25]
Alkali-activate Fly Ash	N-A-S-H	17.75	3.77	N/S = 0.87,H/N = 4.05	[26]
		17.72	3.75	N/S = 1.67,H/N = 2.74	[27]
	Partly Activated Fly Ash	30.50	3.61	N/S = 0.87,H/N = 4.05	[26]
		26.06	0.18	N/S = 1.67,H/N = 2.74	[27]
	Nonactivated Fly Ash	46.63	6.45	N/S = 0.87,H/N = 4.05	[26]
		38.27	10.13	N/S = 1.67,H/N = 2.74	[27]
	Fly Ash	74.01	10.05	N/S = 0.87,H/N = 4.05	[26]
		79.65	16.99	N/S = 1.67,H/N = 2.74	[27]
Portland Cement	Micro porosity	7.45	0.85		[26]
		9.10	2.30		[28]
	LD-CSH	20.16	3.90		[26]
		19.10	5.00		[29]
		21.70	2.20		[30]
		20.20	2.00		[31]
		18.80	4.00		[28]
		22.89	0.76		[32]
	HD-CSH	33.59	2.47		[26]
		29.40	2.40		[30]
		31.00	4.00		[31]
		32.30	3.00		[29]
		31.16	2.51		[32]
	CH	40.74	0.92		[26]
	Cement clinker	122.20	7.85		[32]

(a)

(b)

(c)

(d)

(e)

(f)

(g)

(caption on next page)

Fig. 9. Drying shrinkage simulations at Level I subjected to 50%RH (a) SEM-BSE image with an overall dimension of 276.76 μm × 254.84 μm. (b) After the binary operation to distinguish unhydrated slag. (c) Finite element mesh using OOF2. (d) The trace of the displacement, ranges from 0.000538 μm to 0.295 μm, at free boundary condition. (e) The trace of elastic strain, which ranges from 0 to 0.0027, at free boundary condition (f) The xx component of the total stress, which ranges from −0.0914 in tensile stress to 0.042 in compressive stress, at free boundary condition. (g) The trace of elastic strain, which ranges from 0 to 0.00239 at the confined condition.

addition, an adaptive meshing strategy implemented in the OOF2 preprocessor can provide a satisfying mesh, in which the meshed boundaries reasonably match the original boundary configurations, especially at ITZ range.

4.2. Image acquiring and analyses

Different experimental techniques were implemented to assess geometrical characteristics depending on the size of the phases interested. At Level I (Level II), the BSE-SEM image (Optical image) was used to acquire the microstructure of AAS paste (mortar). The detailed procedure for SEM is similar to the initial steps for FIB, and the detailed image-acquiring procedure for mortar samples can be found in Ref. [20] and hence eliminated here. The main objective of image analysis is to clarify and distinguish each phase from obtained images, and further implemented them in OOF2 code as input files. Grey-level histogram segmentation was employed to identify distinct phases in the image-based microstructures. For instance, at Level I, the sensitivity of BSE imaging to material composition creates phase contrast in the grey-level histogram, facilitating phase differentiation.

4.3. Material mechanical properties

Identification in mechanical properties, mainly elastic modulus, differs as well in Level I and Level II. For Level I, the small-length scale restricts the use of conventional mechanical characterization approaches, and instead, nano-indentation was more prevailingly used to obtain the phase-specific elastic modulus for highly heterogeneous and multi-phase materials. The principle mechanism and detailed information regarding nano-indentation can be found in abundant literature. Table .1 summarizes some reported values of elastic modulus for OPC, AAS, and alkali-activated aluminosilicate materials. In the case of sodium silicate-activated slag, the nano-indentation measured elastic modulus of C–S–H gel is uniformly distributed with identified property. By comparing the activator dosage used in this study with Table .1, an elastic modulus of 27.81 GPa and 80.03 GPa are assigned to C–S–H gel and unhydrated slag, respectively. At Level II, the mechanical properties for aggregate are easy to measure while the elastic modulus of paste can be obtained according to the simulating results from Level I. Typically, the bond phase's mechanical properties are lower than those of bulk cement paste, primarily due to higher porosity. Since the shrinkage simulation at Level II has been realized and elaborated in Ref. [20], the main focus of the present study is on Level I, as well as the correlation between Level I and Level II as a multi-scale scheme as demonstrated in Fig. 1.

4.4. Driving force application

The shrinkage loading consists of applying a uniform volume change in the C–S–H gel using the experimentally measured value by FIB, and no volume change in the unhydrated slag. Similar to the thermal expansion coefficient, the shrinkage coefficient serves as an analogous measure. By imposing a negative temperature load across all meshed elements, finite element simulations were conducted to replicate concrete shrinkage at both micro and macro scales. This method aligns with the idea that while the matrix undergoes volume change due to drying shrinkage, the inclusion impedes its volumetric reduction. The output overall shrinkage coefficient of AAS paste obtained at Level I, can be further used in the shrinkage simulation at Level II using a similar procedure. In this study, a coefficient of thermal expansion of 10μ ε/RH is applied according to the results as shown in Fig. 7. Initially, the initial RH is set to be 100 % (i.e. equivalently to 100 °C), then the samples is subjected to 50 % RH. In addition, two types of boundary are considered in the present research, one is the free boundary and another is the restrained boundary.

4.5. OOF2 simulation results

As shown in Fig. 9(ā̄g), OOF2 can effectively bridge the gap between microscopic and macroscopic dimensions and capture the effect of real microstructures on the shrinkage behaviors of this multi-scale material. The effective modulus of AAS paste is calculated to be 31.54 GPa using OOF2. The displacement field distribution, trace strain distribution, and stress distribution are shown in Fig. 9, respectively. It can be seen that OOF2 is capable of obtaining the strain and stress distribution for heterogeneous materials, while the homogenization approach assumes that free boundary specimens do not experience stress development and the strain is uniform across the section. OOF2 is capable of accurately forecasting stress development and localization in concrete specimens, factoring in how aggregates inhibit the paste phase's volume change due to shrinkage. Since the present study attempts to obtain the overall equivalent shrinkage strain of AAS paste at Level I, OOF2 gives the value of −340.97 με, which is reasonable according to the present problem. It is understandable that the existence of a non-shrink component (slag powder) can restrain the development of paste shrinkage at high magnification, and this is analogous to the case of the aggregate-restrained shrinkage problem [17,33].

5. Conclusions

This paper presents a new method of investigating the drying shrinkage behavior of hydrate products formed in AAS using FIB/ESEM. This novel experimental method allows the in-situ measurement of phase-specific shrinkage and its correlated chemical composition. It shows FIB/ESEM technique can be successfully implemented to cementitious material to prepare phase-specific samples. In addition, a multi-scale simulating model mainly based on OOF2 is proposed, which is demonstrated to be capable of capturing the local stress and strain distribution in microstructure and establishing the gap between different dimensions.

Funding

Institutional review board statement

Not applicable.

Informed consent statement

Not applicable.

Data availability statement

Data associated with my study has not been deposited into a publicly available repository. Data will be made available on request.

CRediT authorship contribution statement

Zhonggou Chen: Conceptualization. **Hua Ding:** Conceptualization. **Guoyi Zhang:** Writing – review & editing, Conceptualization. **Pingtai Chai:** Software.

Declaration of competing interest

The authors declare no conflict of interest.

References

[1] Cf Ferraris, H. Wittmann Folker, Shrinkage mechanisms of hardened cement paste[J], Cement Concr. Res. 17 (3) (1987) 453–464.
[2] P. Bentz Dale, J. Garboczi Edward, A. Quenard Daniel, Modelling drying shrinkage in reconstructed porous materials: application to porous Vycor glass[J], Model. Simulat. Mater. Sci. Eng. 6 (3) (1998) 211.
[3] Jiaping Liu, Qian Tian, Yujiang Wang, Hua Li, Xu Wen, Evaluation method and mitigation strategies for shrinkage cracking of modern concrete[J], Engineering 7 (3) (2021) 348–357.
[4] T. Bakharev, Jg Sanjayan, Y.-B. Cheng, Effect of admixtures on properties of alkali-activated slag concrete[J], Cement Concr. Res. 30 (9) (2000) 1367–1374.
[5] Collins Frank, Jg Sanjayan, Effect of pore size distribution on drying shrinking of alkali-activated slag concrete[J], Cement Concr. Res. 30 (9) (2000) 1401–1406.
[6] Hailong Ye, Cartwright Christopher, Rajabipour Farshad, Radlińska Aleksandra, Understanding the drying shrinkage performance of alkali-activated slag mortars[J], Cement Concr. Compos. 76 (2017) 13–24.
[7] M. Rashad Alaa, W.M. Morsi, A. Khafaga Sherif, Effect of limestone powder onmechanical strength, durability and drying shrinkage of alkali-activated slag pastes[J], Innovative Infrastructure Solutions 6 (2) (2021) 1–12.
[8] M. Rashad Alaa, Influence of different additives on the properties of sodium sulfate activated slag[J], Construct. Build. Mater. 79 (Mar.15) (2015) 379–389.
[9] Hailong Ye, Radlińska Aleksandra, Shrinkage mechanisms of alkali-activated slag[J], Cement Concr. Res. 88 (2016) 126–135.
[10] Hailong Ye, Radlińska Aleksandra, Shrinkage mitigation strategies in alkali-activated slag[J], Cement Concr. Res. 101 (2017) 131–143.
[11] Cm Neubauer, Tb Bergstrom, K. Sujata, Y. Xi, Ej Garboczi, Hm Jennings, Drying shrinkage of cement paste as measured in an environmental scanning electron microscope and comparison with microstructural models[J], J. Mater. Sci. 32 (24) (1997) 6415–6427.
[12] Bissonnette BenoıT, Pierre Pascale, Pigeon Michel, Influence of key parameters on drying shrinkage of cementitious materials[J], Cement Concr. Res. 29 (10) (1999) 1655–1662.
[13] Img Bertelsen, C. Kragh, G. Cardinaud, Lm Ottosen, G. Fischer, Quantification of plastic shrinkage cracking in mortars using digital image correlation[J], Cement Concr. Res. 123 (2019), 105761.
[14] Kheir Judy, A. Klausen, Ta Hammer, De Meyst Laurence, Hilloulin Benoit, Kim Van Tittelboom, Loukili Ahmed, De Belie Nele, Early age autogenous shrinkage cracking risk of an ultra-high performance concrete (UHPC) wall: modelling and experimental results[J], Eng. Fract. Mech. 257 (2021), 108024.
[15] Cm Neubauer, M. Jennings Hamlin, The use of digital images to determine deformation throughout a microstructure Part II Application to cement paste[J], J. Mater. Sci. 35 (22) (2000) 5751–5765.
[16] Qing Liu, Jiakang Zhang, Yuewei Su, Xianjun Lv, Variation in polymerization degree of C-A-S-H gels and its role in strength development of alkali-activated slag binders[J], J. Wuhan Univ. Technol. 36 (6) (2021) 871–879.
[17] Ippei Maruyama, Sasano Hiroshi, Strain and crack distribution in concrete during drying[J], Mater. Struct. 47 (3) (2014) 517–532.
[18] Wenyan Zhang, Zakaria Mohamed, Yukio Hama, Influence of aggregate materials characteristics on the drying shrinkage properties of mortar and concrete[J], Construct. Build. Mater. 49 (2013) 500–510.
[19] De Larrard Thomas, Bary Benoit, Erwan Adam, Kloss Francis, Influence of aggregate shapes on drying and carbonation phenomena in 3D concrete numerical samples[J], Comput. Mater. Sci. 72 (2013) 1–14.
[20] Moon Jae Heum, Shrinkage, Residual Stress, and Cracking in Heterogeneous materials[M], ProQuest, 2006.
[21] Tc Chu, Wf Ranson, Ma Sutton, Applications of digital-image-correlation techniques to experimental mechanics[J], Exp. Mech. 25 (3) (1985) 232–244.

[22] Bing Pan, Kemao Qian, Huimin Xie, Asundi Anand, Two-dimensional digital image correlation for in-plane displacement and strain measurement: a review[J], Meas. Sci. Technol. 20 (6) (2009), 062001.

[23] Eberl Christoph, R. Thompson, D. Gianola, W. Sharpe Jr., K. Hemker, Digital Image Correlation and tracking[J]. MatLabCentral, Mathworks File Exchange Server, FileID, 2006, 12413.

[24] F. Feldman Rolf, Mechanism of creep of hydrated Portland cement paste[J], Cement Concr. Res. 2 (5) (1972) 521–540.

[25] S. Gebregziabiher Berhan, Peethamparan Sulapha, Characterization of Alkali Activated Slag Gel Using Nano-Indentation; Proceedings of the 3rd International Conference on Sustainable Construction Materials and Technology - SCMT2013, Ktoto, Japan, F, 2013 [C].

[26] Němeček Jiří, Vít Šmilauer, Kopecký Lubomír, Němečková Jitka, Nanoindentation of alkali-activated fly ash[J], Transport. Res. Rec.: J. Transport. Res. Board 2141 (1) (2010) 36–40.

[27] Němeček Jiří, Vít Šmilauer, Kopecký Lubomír, Nanoindentation characteristics of alkali-activated aluminosilicate materials, Cement Concr. Compos. 33 (2) (2011) 163–170.

[28] G. Constantinides, F.-J. Ulm, The Elastic Properties of Calcium Leached Cement Pastes and Mortars: a Multi-Scale Investigation [R], MIT CEE, 2006.

[29] J. Dejong Matthew, Ulm Franz-Josef, The nanogranular behavior of CSH at elevated temperatures (up to 700 C)[J], Cement Concr. Res. 37 (1) (2007) 1–12.

[30] Constantinides Georgios, Ulm Franz-Josef, The effect of two types of CSH on the elasticity of cement-based materials: results from nanoindentation and micromechanical modeling[J], Cement Concr. Res. 34 (1) (2004) 67–80.

[31] P. Acker, in: F.-J. Ulm, Z. Bažant, F. Wittman (Eds.), Micromechanical Analysis of Creep and Shrinkage Mechanisms Proceedings of the, Creep, Shrinkage and Durability Mechanics of Concrete and Other Quasi-Brittle Materials, Elsevier, Oxford, UK, F, 2001 [C].

[32] Paramita Mondal, P. Shah Surendra, Marks Laurence, A reliable technique to determine the local mechanical properties at the nanoscale for cementitious materials[J], Cement Concr. Res. 37 (10) (2007) 1440–1444.

[33] Idiart Andrés, Bisschop Jan, Antonio Caballero, Lura Pietro, A numerical and experimental study of aggregate-induced shrinkage cracking in cementitious composites[J], Cement Concr. Res. 42 (2) (2012) 272–281.